Book of Tutorials and Abstracts

European Microbeam Analysis Society

EMAS 2023

17th

EUROPEAN WORKSHOP

on

MODERN DEVELOPMENTS AND APPLICATIONS IN MICROBEAM ANALYSIS

7 to 11 May 2023
at the
Jagiellonian University, Auditorium Maximum
Krakow, Poland

Under the auspices of the Rector of the
Jagiellonian University, Krakow, Poland
Organised in collaboration with the
Institute of Metallurgy and Materials Science of
the Polish Academy of Sciences, Krakow, Poland

EMAS
European Microbeam Analysis Society eV
www.microbeamanalysis.eu/

This volume is published by:
European Microbeam Analysis Society eV (EMAS)
EMAS Secretariat
c/o Eidgenössische Technische Hochschule, Institut für Geochemie und Petrologie
Clausiusstrasse 25
8092 Zürich
Switzerland

ISBN 978 90 8227 6961
NUR code: 972 – Materials Science

ALMOST 100 YEARS OF X-RAY KOSSEL DIFFRACTION AND ITS ADVANTAGES VERSUS THE EXCLUSIVE APPLICATION OF EBSD: FROM THE PREDICTION TO CURRENT DEVELOPMENTS

A tribute to the memory of Priv.-Doz. Dr. rer. nat. Siegfried Däbritz

Enrico Langer

Technische Universität Dresden, Institute for Semiconductor and Microsystems
Nöthnitzer Strasse 64, 01187 Dresden, Germany
e-mail: langer@physik.tu-dresden.de

Enrico Langer obtained his Dipl.-Phys. degree in physics from the Technische Universität Dresden in the fields of surface and microstructure characterisation using SEM, EPMA as well as μ-X-ray Kossel and pseudo-Kossel diffraction. In 2005 he earned his PhD in natural sciences dealing with the effect of crystal defects on the above mentioned diffraction methods at the same institution under supervision of Priv.-Doz. Dr. habil. Dr. S. Däbritz. Since 2013 he is a permanent staff scientist and fully involved in the teaching responsibilities of the Institute of Semiconductors and Microsystems at the TU Dresden. He gives lectures on material sciences both for the microelectronics and microsystems as well as for micro-mechatronics. Meanwhile having become an authority in this field, his research focuses on the development of novel methods using these special μ-X-ray diffraction techniques in combination with EBSD, particularly for the characterisation of crystal defects and the real structure in the SEM. Now a lifetime member, he joined the EMAS in 1998. Since 2011 he is Treasurer of the EMAS. He has published a review paper on Kossel patterns and frequently as the main author, more than 30 refereed scientific articles in international journals with a resulting Hirsch factor of 15 as well as 60 contributions to national and international conferences in proceedings.

1. ABSTRACT

The year 2024 will mark the 100th anniversary of the prediction of X-ray interferences from lattice sources by W. Kossel. The μ-X-ray Kossel diffraction (μXKD) can be easily applied in combination with EBSD as additional complementary diffraction method in a SEM or in a microprobe. It has the highest informational content and precision compared to conventional diffraction methods. It is simply possible to use one single scintillator CCD detector combination to observe both diffraction methods, which will be especially discussed more in detail here, as our group has successfully demonstrated over 25 years. An overview of selected applications will be given, besides of precise local lattice constants measurements, the determination of phase angles of the structure factor and polar planes in non-centrosymmetric crystals at the semiconductors GaP and GaAs, the estimation of dislocation densities in sinter model materials, the thermal conductivity, thermal expansion coefficients and the phase identification in Au-Ti diffusion zones. Finally, novel developments of the X-ray Kossel diffraction will be presented as a new simply method to evaluate orientation relationships and its application in shape memory alloys and the explanation of observed unusual Kossel line splitting's, for the first time.

2. INTRODUCTION

2.1. Almost the 100th anniversary of the prediction of the interference of the characteristic X-rays in a crystal at Kiel University

At the discovery of the diffraction of X-rays by crystals by M. von Laue *et al.* in 1912, initially the interference of fluorescent radiation excited in the crystal had been erroneously supposed to be the cause of the diffraction of X-rays by crystals. M. von Laue recognised quickly that the direct diffraction of the incident X-rays is the right interpretation. This idea of the diffraction of the secondary radiation was rejected again and was not recognised as a new interference method until W. Kossel predicted in 1924 the interference of characteristic X-rays in the crystal, in which the self-radiation is excited, the so-called X-ray interferences from lattice sources [1]. Ten years later this X-ray interference effect was proven by W. Kossel *et al.* in 1934 [2].

2.2. Principle of the lattice source X-ray interferences or X-ray Kossel diffraction

The Kossel effect exploits the emitted characteristic X-rays within the investigated crystalline volume. Thereby, the excitation is mainly performed with electrons [2-3], but also with X-rays [4], protons [5], ions [6] or synchrotron X-ray [7-8], respectively. Later the X-ray excitation of Kossel patterns with a focussing polycapillary lens using an X-ray fluorescence (XRF) spectrometer [9] and with a compact X-ray source at a secondary electron microscope (SEM) was shown [10]. In the future, the excitation by an X-ray free-electron laser is conceivable [11]. In directions satisfying Bragg law rotationally symmetric sharp cones appear, the so-called

Kossel cones, named to W. Kossel's honour, see Fig. 1. Nowadays, on a planar charged-couple detector (CCD) detector [13-17] pure dark and bright Kossel lines appear and such with a bright-dark fine structure (see line profile of 220 reflection in Fig. 6), indicating complex interference phenomena, which have to be dealt by the dynamical theory of X-ray diffraction [12]. The characteristic X-rays of all chemical elements are excited for the Kossel effect, for example at a Ni_2MnGa monocrystal mainly the Ni-K$\alpha_{1/2}$-radiation with high intensity and this then interferes, see Fig. 2 on the right side. In fact, also the Mn- and Ga-radiation is excited in this case.

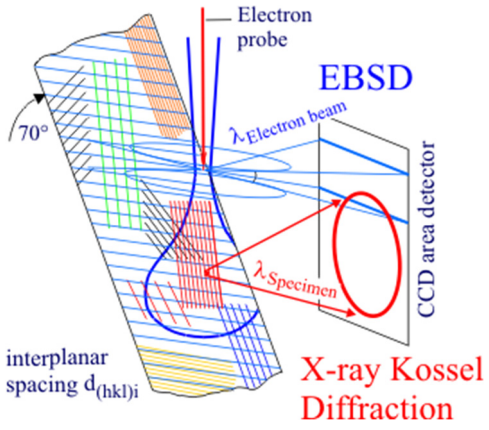

Figure 1. Basic principle of the Kossel effect with electron excitation in combination with EBSD. The Kossel curves are conic section: circles, ellipses, parabolas, and hyperbolas, but only one Kossel circle reflection is shown.

2.3. Motivation to apply additional the X-ray Kossel μ-diffraction versus only EBSD

It has become apparent that electron backscatter diffraction (EBSD) is an advantageous method with high lateral resolution and fast mapping speed for phase discrimination, orientation determination and texture analysis as well as is characterised by an increasing relative accuracy through the development of the cross-correlation method by Wilkinson *et al.* [18, 19]. Recently, the intensity simulation by the dynamical diffraction theory by Winkelmann [20. 21] led to further crystal information, like the point-group sensitive orientation mapping on non-centrosymmetric phases by Nolze *et al.* [22], see Table 1. However, the X-ray Kossel diffraction has a high informational content, and provides information also on the crystal symmetry and crystal structure, superstructures, exact orientations and misorientations, on dislocation densities, allows the precise determination of local lattice constants up to a relative accuracy of 10^{-5}, of tetragonal distortions with a shown accuracy of $\Delta(c/a) = \pm 0.0006$ [23] as well as residual stresses all three in the μ-range. For the last-mentioned parameters, the attainable precision is unreachable with EBSD, see Tables 1 and 2. Therefore, the Kossel technique is an extremely valuable additional method in combination with EBSD. Typical measurements can start with an EBSD mapping and in a second step some Kossel patterns on problematic

(e.g., non-identified black pixel regions) or other selected measuring points will provide missing or more precise additional crystal information. Table 1 summarises the most important crystal information, which can be determined by X-ray Kossel diffraction compared to EBSD.

Table 1. Comparison of crystal parameters and applications of Kossel compared with EBSP.

Crystal parameters and applications (current state of research in 2023)	Kossel	EBSD
· Automated crystal orientation mapping and texture analysis		●●●
· Automated pattern quality mapping		+++
· Automated phase discrimination map		++
· Polarity-sensitive orientation mapping on non-centrosymmetric phases		++
· Polar plane distinction on non-centrosymmetric crystals	+++	++
· Phase identification	++	+
· Crystal structure determination	++	+
· Symmetry determination, e.g. tetragonal distortion	+++	+
· New formation of phases and phase change in the high- and	++	+
low temperature range	++	+
· Exact determination of crystal orientations: ± 0.01°	+++	++
· Residual stress measurements	+++	+
· Precise lattice constant determination: $\Delta a/a \approx 10^{-5}$	●●●	
· Phase determination from the structure factor	++	
· Direct estimation of dislocation densities: (10^6 - 10^{10}) cm^{-2}	++	
· Proof of mechanical tensions and deformations	+++	
· Determination of expansion coefficients	+++	
· Indirect determination of chemical concentration	++	
· Detectability, location of crystal defects	+	

●●●: main application; +++: excellent; ++: very good; +: possible. Updated table from [16].

2.4. Details of the CCD detection for the X-ray Kossel microdiffraction

For all those interested in EBSD also the X-ray Kossel diffraction could be exciting as a further additional µ-diffraction method, which can be easily combined with EBSD. Since there exist no commercial system as far as the author do know, important detail information about the applied scintillator CCD area detector combination to observe X-ray Kossel diffraction patterns should be given in the following, which Däbritz and Langer started to develop in the year 1998 [15-17].

Table 2. Comparison of the precision of both diffraction methods.

	Kossel Diffraction	Electron Backscatter Diffraction
• Symmetry determination, e.g. tetragonal distortion		
Precision:	$\Delta(c/a) = \pm 0.0006$ Ullrich et al. [23]	$\Delta(c/a) = \pm 0.01$ Nolze et al. [27]
Lowest detectable deviation	$c/a = 1.002$ Ullrich et al. [23]	$c/a = 1.01$ Nolze et al. [27]
Evaluation method:	multiple line intersections	
• Precise lattice constant determination		
Precision:	$\Delta a/a \approx 10^{-5}$ in special cases: $3 \cdot 10^{-6}$ [24]	$\Delta a/a \approx 10^{-2}$ Method is too imprecise
• Crystal lattice orientation determination		
Absolute orientation precision:	0.1°	~1°
Evaluation method:		standard Hough transform
Relative orientation precision:	0.01°	0.5° - 0.1°
Evaluation method:		standard Hough transform
		0.01° [18, 19]
Evaluation method:		pattern cross-correlation [18, 19]
• Residual stress measurements		
Detailed information	Allows absolute and relative residual stress measurements, that means distinguishable residual stress measurements of the 1st, 2nd and 3rd kind	Allows residual stress measurements relative to a reference point in the same crystallite, that means residual stress measurements of the 3rd kind
Precision:	10^{-5}	10^{-4} [18, 19]
Evaluation method:	precision compensation method [25]	pattern cross-correlation based [18, 19]
Highlight:	Residual stress mappings [26]	

2.4.1. Basic information about image detection, formats and developed image software.

- At least a resolution of 1,280 × 1,024 pixels of the CCD detector was required;
- 8-bit images are insufficient for Kossel patterns, at least 12-bit (4,096 grey values) or higher were needed;
- A 16-bit bitmap format (*.b16) is used to save the 12-bit bitmap CCD Kossel patterns, which is built up like the standard 8-bit image format, we did use the additional 4 bits for a text documentation for all observation parameters and a description of the sample;

- A special software was required in order to observe and process the digital images, which were developed in-house in the programming language C++ and is called "SENSICAM", whereby only the programming of the observation of the Kossel patterns was on the basis of a developer Kit belonging to the CCD detector;
- The CCD area detector combined with the developed software allow an integration time of at least 1 - 5 min for X-ray Kossel patterns and more for special high- quality patterns (typical 6 - 8 min);
- Similar to EBSD the software controls the SEM CamScan CS44 to switch between scanning for the Kossel background pattern and the concentration of the electron beam on one spot to generate the Kossel diffraction pattern;
- In order to see the Kossel lines, it is necessary to subtract or to normalize the 12-bit bitmap Kossel patterns from the Kossel background pattern by analogy to the procedure for EBSD, see Fig. 2;
- Identical with EBSD for polycrystalline samples a scanning over different orientated grains is used for the background pattern, whereas for monocrystals the sample is rotated during the integration time of the background pattern to blur the Kossel lines, as can be seen on a Ni_2MnGa monocrystal in Fig. 2;
- It is important to achieve a perfect agreement between Kossel and background pattern by maintaining especially the same absorption current on average;
- For an excellent Kossel pattern, the integration time must be optimized by the grey value histogram, which should be as wide as possible, but the development of the Gaussian shaped peak on the right side have to be avoided, since it is a sign of a to high exposed pattern, see Fig. 3, which are caused by scattered electrons which appear at long integration times in dependence of the absorber foil thickness for the backscattered electrons.

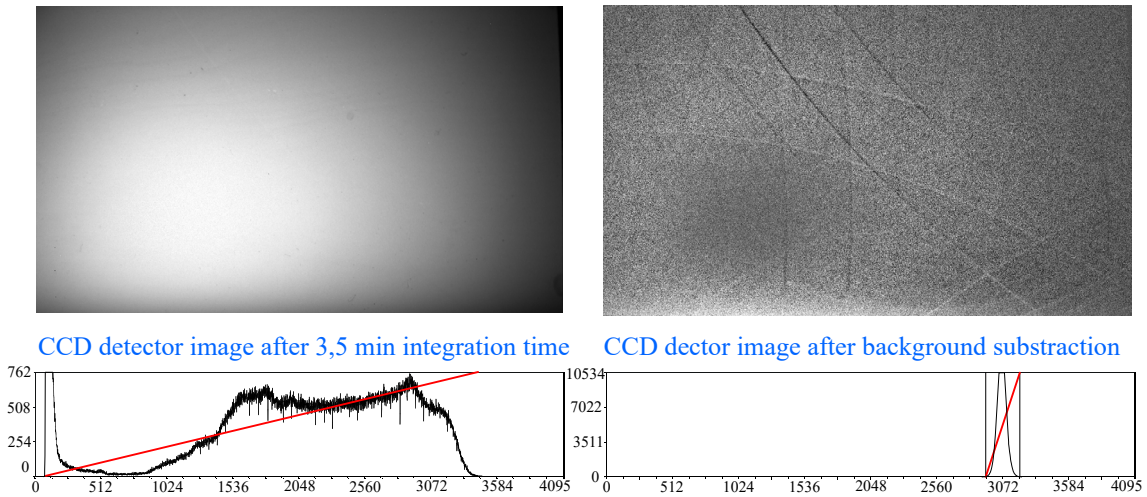

Figure 2. Comparison between Kossel line CCD pattern left and background subtracted Kossel pattern on the right side of a Ni_2MnGa monocrystal with corresponding grey value histogram in each case (acceleration voltage: 25 kV, absorption current: 0.1 µA, observed with phosphor type P43 and 3 gold foils each with 200 nm thickness were used between sample and screen in order to avoid the backscattered and diffracted electrons).

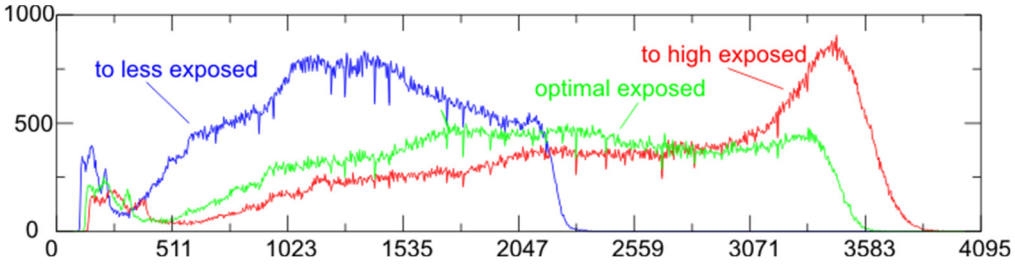

Figure 3. Grey value histogram of a to less, to high and optimal exposed Kossel pattern.

2.2.2. Optimisation of the phosphor scintillator. Different phosphors were tested as listed in Table 3 and additional from the material P22G ZnS:Cu,Al,Au screens with varied superficial density produced. The optimal screen both for X-ray Kossel diffraction and EBSD was from the type P43 with the in Fig. 4 presented transmission geometry with Al reflex layer and the there given parameters.

Table 3. Arrangement of tested phosphors (www.apace-science.com/ast/phsophor.htm)

Type	**Composition**	**Maximum emission λ/nm**	**Decay time to 10 % intensity**	**Particle size / µm**	**Energetical efficiency / %**
P20	ZnCdS: Ag, Cu	530 (green)	80 µs	2.5 - 10	22
P22G	ZnS: Cu, Al, Au	540 (green)	35µs	4 -10	22
P43	Gd2O2S: Tb	545 (green)	1.5 ms	2.5 - 25	15

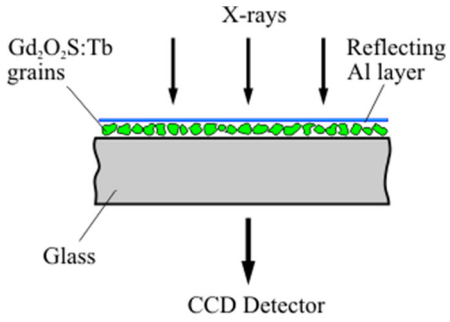

Type: Phosphor scintillator P43: Gd_2O_2S:Tb	
Superficial density	20 mg/cm²
Average particle size	4 µm
Al reflection layer	50 nm
Glass substrate size	(100×80×2) mm²
Usable phospor area	(98×78) mm²
Effective used section	(90×70) mm²

Figure 4. Schematic setup and data for X-ray Kossel diffraction optimised screen.

2.2.3. Filter foils for the X-ray Kossel pattern observation. In order to avoid backscattered and diffracted electrons to form EBSP for the Kossel pattern detection, between one (for a fast detection of 60 s) and up to three gold filter foils (high quality) were used between sample and screen; each with a thickness of 200 nm.

3. *GREAT VARIETY OF APPLICATIONS*

3.1. Determination of the phase angle of the structure factor

For conventional X-ray diffraction methods in which the X-ray source lies outside of the crystal, by the experimental measured intensity $I_{hkl} \sim |F(hkl)|^2$ of an X-ray reflection only the modulus of the structure factors |F(hkl)| and *not* the phase angle α(hkl) of the structure factor F(hkl) can be evaluated (phase problem of the crystal structure analysis with X-rays or electron beams): $F(hkl) = |F(hkl)|\, e^{i \cdot \alpha(hkl)}$.

A direct solution lies in the Kossel lines, which show a remarkable bright-dark fine structure in the line profiles, their intensity was calculated by means of dynamical X-ray diffraction by Max von Laue [28, 29]. Already by H. Ott [30] was suggested to apply these fine structure for the experimental direct determination of these scatter phase angles at the crystal structure analysis. Blau *et al.* [31] have discussed the concrete evidence concerning mainly the sign of the structure factor at experimental examples. The determination of the phase information that means the phase angle especially at mixed structure factors by comparison between theoretical calculated and experimental Kossel line profiles considering the absorption were shown by Stephan *et al.* [32, 33] at many examples, like for instance Fe, ZnS etc., but also as below for GaAs.

Brümmer and Nieber [34] investigated the fine structure of the Kossel lines in dependence on the phase in the symmetric Laue case, see Fig. 5, with the help of measured photometer curves, especially in GaP and GaAs at the reflections (220) and (111) Ga-Kα, see Fig. 6. Kossel line fine structure and corresponding readable phase angles are listed in Table 4.

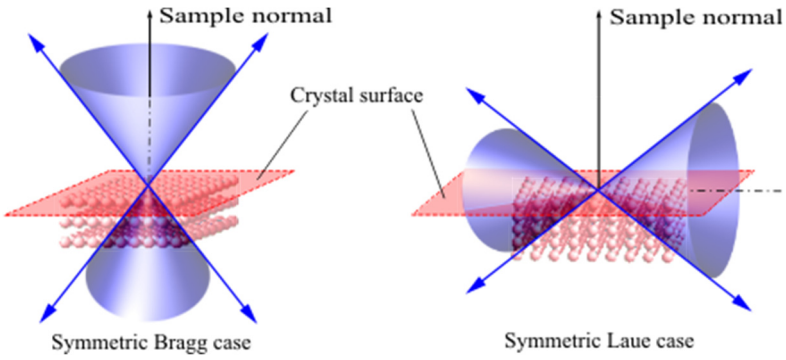

Figure 5. Special geometry cases of Kossel cones relative to the crystal surface.

Hutton *et al.* [35] investigated the feasibility to exploit Kossel lines in the Bragg case for the measurement of the phase angle. The line profiles of Ga (111) and Ga (333) Kossel reflections on GaAs were exemplary calculated for this purpose and furthermore they suggested the

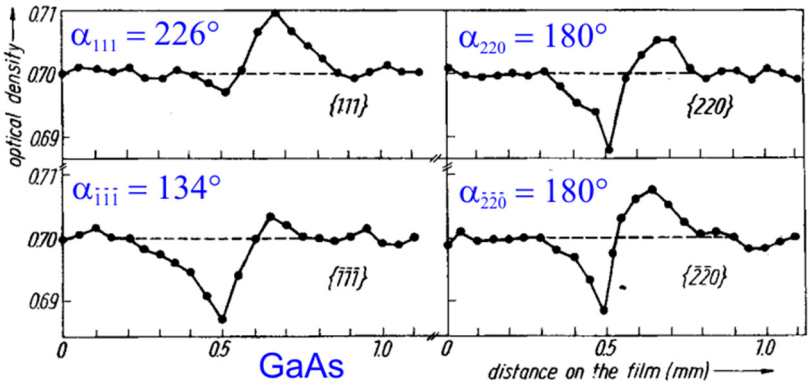

Figure 6. Two selected examples of photometer curves of the {1 1 1}, {$\bar{1}$ $\bar{1}$ $\bar{1}$} and {2 2 0}, {$\bar{2}$ $\bar{2}$ 0} Ga-Kα type Kossel reflections in GaAs with the phase α(hkl) assigned to the reflections in each case inserted on the left side above from [34].

Table 4. From the fine structure of the Kossel line profile simply readable qualitative phase angle: 0° ≤ phase angle α(hkl) ≤ 360° in the symmetric Laue case from [34].

Fine structure of the Kossel line profiles	**Readable phase angle $\alpha_{(hkl)}$**
mainly dark Kossel line (see Fig. 6)	α(hkl) > 180°
mainly bright Kossel line (see Fig. 6)	α(hkl) < 180°
symmetric bright-dark Kossel line fine structure	α(hkl) ≅ 180°

synchrotron excitation. Recently the experimental determination of the phases α(hkl) of the structure factor from measured line profiles on further Kossel reflections of GaAs succeeded quantitatively by synchrotron excitation in [36].

3.2. Polar plane distinction on non-centrosymmetric semiconductor crystals

Analysing the crystal structure symmetries and their determination play an important role. Conventional X-ray diffraction methods cannot prove an inversion centre, as expressed in the Friedel's rule, which states, that for X-ray diffraction the intensity of the reflections h k l and $\bar{h}\ \bar{k}\ \bar{l}$ is identical. Also, for non-centrosymmetric crystals, i.e., do not have a centre of symmetry apply: $I_{\bar{h}\,\bar{k}\,\bar{l}} = I_{h\,k\,l}$.

Max von Laue's assumption of the Kossel effect on non-centrosymmetric crystals was, that it will be possible to distinguish between the directions < h k l > and < $\bar{h}\ \bar{k}\ \bar{l}$ > by the Kossel effect, i.e., Friedel's law is violated here, which was verified in [37, 34].

The features in the interference phenomena which appear in non-centrosymmetric compared to centrosymmetric crystals are highly suitable for the determination of polar axes in non centrosymmetric crystals by the Kossel effect and for an unambiguous distinction between non-centrosymmetric and centrosymmetric crystals [37, 34].

It can be seen particularly clear at the non-centrosymmetric III-V-semiconductor GaP of Fig. 7 with zinc blende structure, since for P-Kα-radiation (λ = 0.6154 nm [38]) only 8 reflections of the {111}-type occur. The bright Kossel circle emerges on the side of the small monocrystal plate with the Ga atoms (A-face). The dark circle arises at the exposure of a Kossel pattern on the reverse side with the P atoms (B-face) [39]. Further polarities were determined on the III-V-compound semiconductors GaAs, GaP and InP for optoelectronic components by Nolze *et al.* [40].

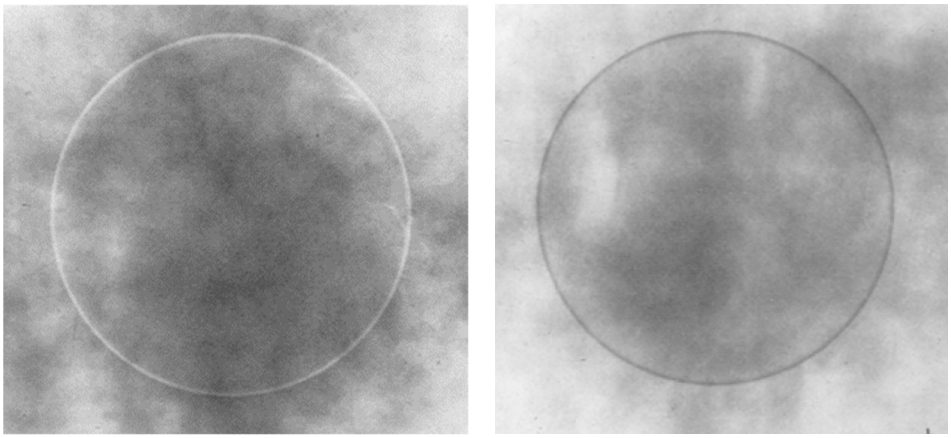

Figure 7. Kossel pattern of GaP, left: 111-P-Kα circle reflection on the (111) and right $\bar{1}\,\bar{1}\,\bar{1}$-P-Kα reflection on the $(\bar{1}\,\bar{1}\,\bar{1})$ crystal surface is clearly distinguishable [39].

3.3. Direct estimation of dislocation densities: (10^6 - 10^{10}) cm^{-2}

The line width of Kossel patterns clearly changes in the range of 10^6 to 10^{10} dislocations per cm^2. In order to estimate dislocation densities in the µ-range by the Kossel technique calibration samples of the same material with known different dislocation densities are required, to calibrate the correlation between dislocation density and line width. For measurement of the line width in the crystal volume to be investigated and on the calibration samples an identical point of the Kossel line in the same reflection system section must be utilised [41]. Because of the high symmetry such as for the cubic crystal structure this is easy to implement. Starting from a dislocation density of 10^9 cm^{-2} it was additionally necessary to adjust the same take-off angle of the measuring position on the reflection to the sample surface [41].

Measurements on reflections of the type {1 1 1} of monocrystalline Cu balls on (1 1 1)-oriented Cu single crystals in the sintering contact region especially at the [$\bar{1}\,\bar{1}\,\bar{2}$] pole were carried out by Ullrich *et al.* [41] and Herenz *et al.* [42], which are summarized in Fig. 8. At dislocation densities between 10^9 and 10^{10} cm^{-2} a splitting of {111} Kossel lines were observed, whereby this appearance was discussed as typical for this range [41].

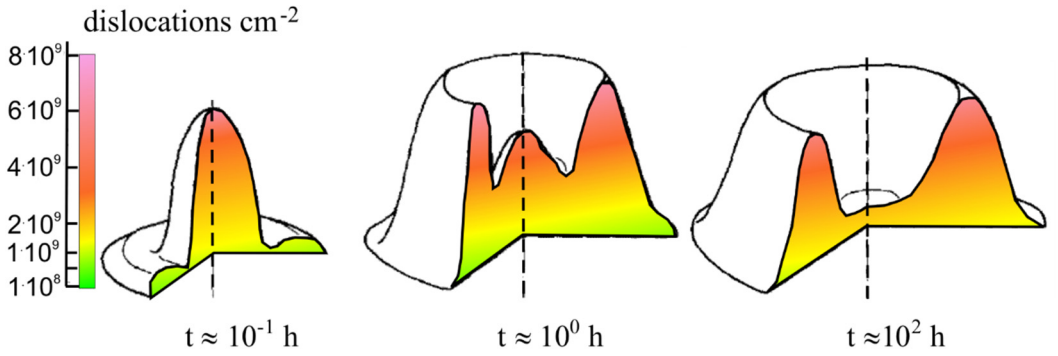

Figure 8. Idealised 3d representation of the by means of the Kossel diffraction measured dislocation density distribution from [41] depending on the sintering time t at a sinter temperature of T = 900 °C.

3.4. Estimation of thermal conductivity in the micro-range

The comparison of experimentally determined temperature increases by means of measurement the lattice constant changes for different absorption currents (constant accelerating voltage) with theoretical ascertained values, allows with known expansion coefficients α from literature the estimation of the thermal conductivity λ:

with $\Delta T = \frac{\Delta a}{\alpha \cdot a_0}$ and $\Delta T = \frac{3 \cdot P}{2 \cdot d \cdot \pi \cdot \lambda}$; it follows $\lambda = \frac{3 \cdot \alpha \cdot a_0 \cdot P}{2 \cdot d \cdot \pi \cdot \Delta a}$,

where ΔT is the temperature increase, Δa is the lattice constant change between two different absorption currents measured by the Kossel technique, d is the diameter of the electron probe and P is the electrical power [43]. The lattice constant a0 of the analysed area without a heating by the electron probe can be extrapolated for $i \rightarrow 0$ by the linear experimentally measured connection between lattice constant a and absorption current i. The conductivities λ of the compounds FeAl, $MgCu_2$ and the superconductor v3Si were estimated by Däbritz [43] and are summarised in Table 5.

3.5. Determination of thermal expansion coefficients

Vice versa, for a known thermal conductivity λ from the literature also a determination of the thermal expansion coefficients α is easily possible. In Table 6, the essential results of thermal expansion coefficient and lattice constant measurement by high-temperature Kossel investigations attained by Däbritz and Ullrich are listed [43-45].

Table 5. Estimation of thermal conductivity λ in the µ-range by Kossel diffraction [43].

substance	U /kV	i /µA	d /µm	$\overline{T}$ /K	$\alpha \cdot 10^{-6}$ /K^{-1}	$\Delta a/(\alpha \cdot a_o)$ /K	λ /$W \cdot mK^{-1}$
FeAl	60	2.8	35	293	18	81.3	28.2
FeAl	60	1.0	35	293	18	38	21.5
$MgCu_2$	60	1.0	35	293	31.5	3.6	230
V_3Si (grain 1)	50	2.3	50	100	4	205	5.4
V_3Si (grain 2)	50	2.7	50	100	4	230	5.6
V_3Si (grain 3)	50	4.0	50	100	4	347	5.5
V_3Si (grain 4)	50	2.0	50	170	4	159	6.0

Table 6. Overview of high-temperature Kossel investigations regarding lattice constant changes for expansion coefficient measurements [43-45]; α: thermal expansion coefficient ascertained, a: lattice constant determined.

Material	*Temperature range/°C*	*Measured* variable	***Relative precision*** of the a-determination
Fe	20 to 850	a(T), α(T)	$1 \cdot 10^{-4}$
Ni	20 to 110	a(T), α(T)	$3 \cdot 10^{-5}$
Cu	20 to 80	a(T), α(T)	$3 \cdot 10^{-5}$
Fe_3O_4	20 to 856	a(T), α(T)	$3 \cdot 10^{-4}$
Fe_3Al	20 to 100	a(T), α(T)	$3 \cdot 10^{-5}$
$MgCu_2$	20 to 80	a(T), α(T)	$3 \cdot 10^{-5}$

3.6. Phase identification in Au-Ti diffusion zones by the Kossel diffraction

The Au-Ti system was studied due to their significance for the hardness of gold jewellery [46]. Multiphase diffusion zones in the Au-Ti alloys should serve as an example for the advantageous characterisation of a large variety of different crystal phases, which were investigated by the Kossel technique [47]. The presented sample was prepared by annealing a compact Au-Ti sandwich at 1,073 K for 216 h [47]. Figure 9 shows a SEM micrograph of the diffusion zone. The composition of each intermetallic compound has been measured by energy-dispersive X-ray spectrometry (EDS) in electron probe microanalysis (EPMA), whereas the plotted crystal phases were identified and the crystal orientations were determined by the Kossel diffraction [47]. In Fig. 10, the sphere models of Au_4Ti, Au_2Ti and $AuTi_3$ can be seen, which are oriented in the direction of the measured crystal orientation in diffusion direction, whereby the special crystal orientation of the Au_4Ti crystal illustrates the similarity of the "open" directions to Au_2Ti, if one neglects the atom species [47]. Figure 11 shows the simulated Kossel reflection system of Au_2Ti with the self-developed programme KOPSKO 2.0 [48]. Table 7 gives the overview of the crystal data of different phase.

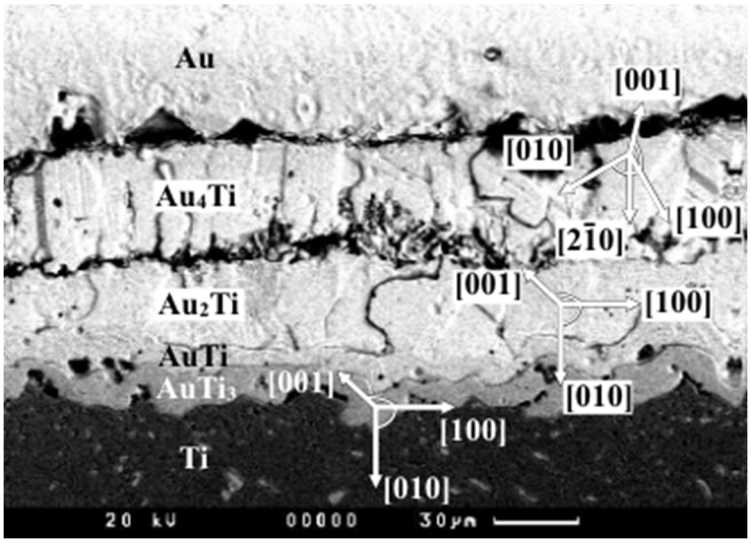

Figure 9. With EDS and Kossel technique determined crystal phases Au_4Ti, Au_2Ti, and $AuTi_3$ with plotted crystal orientation shown within the diffusion zone of the corresponding scanning backscattered electron micrograph [47].

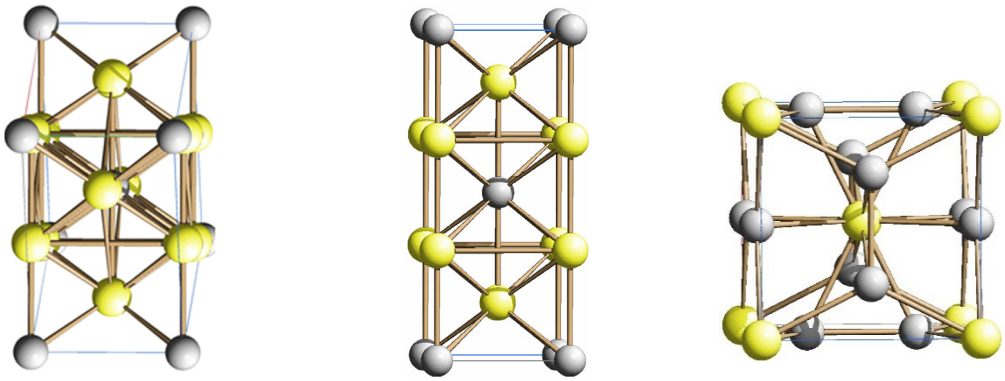

$Au_4Ti \approx [2\bar{1}0]$ direction $Au_2Ti \approx [100]$ direction $AuTi_3 \approx [100]$ direction

Figure 10. Spherical model representation of the relation between the most "open" crystal orientations of grains and the growth or diffusion direction of the crystal phases, which were found [47] (Au – yellow; Ti –grey). A similar dependence was proved in the Cu-Sn diffusion system also in the group of Däbritz *et al.* [49].

Table 7. Overview of the crystallographic data of the crystal phases.

Au_4Ti	tetragonal body centred, Ni_4Mo-type, space group: I4/m (No.: 87)
Au_2Ti	tetragonal body centred, $MoSi_2$-type, space group: I4/mmm (No.: 139)
$AuTi_3$	primitive cubic, A15, β-W or Cr_3Si-tpye, space group: P m $\bar{3}$ n (No. 223)

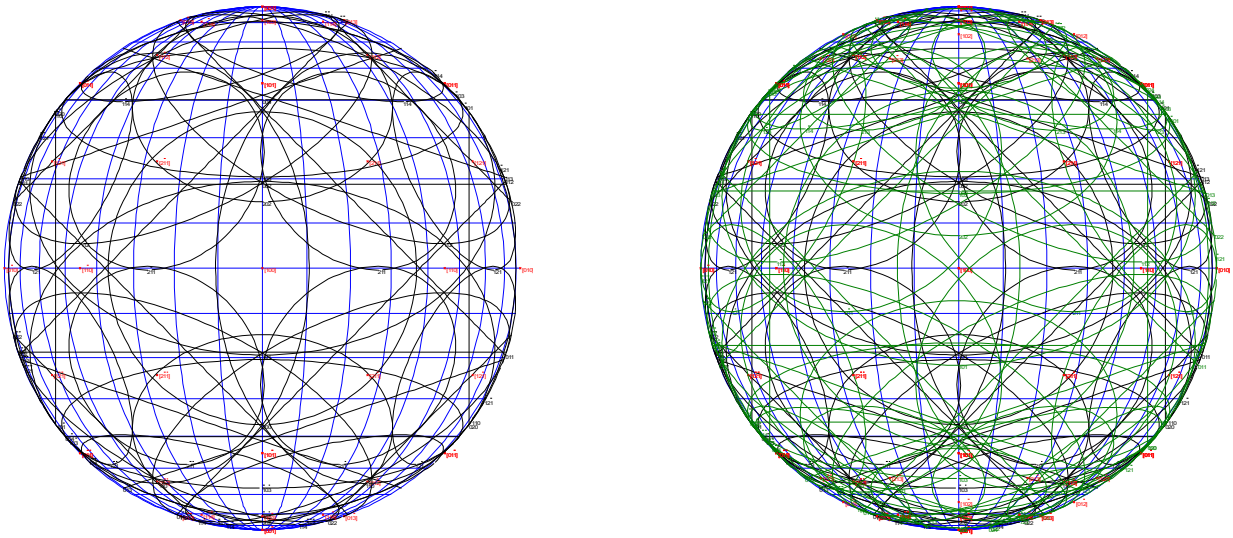

Figure 11. Simulated Kossel reflections of Au_2Ti at the [100] pole, left using only Ti-Kα_1 (black) and on the right side additionally with Ti-Kβ_1 radiation (green) in parallel projection with the program KOPSKO 2.0.

4. *EXTENSION OF THE KOSSEL INVESTIGATIONS TO A FURTHER MATERIAL CLASS OF FERROMAGNETIC SHAPE MEMORY ALLOYS*

4.1. Introduction in the material

As far as known by the author only one conventional shape memory alloy of the system Cu-Al-Be was investigated by the Kossel method up to now and is documented in a few publications [50, 51]. In 1996, the magneto-striction was measured by Vail'ev *et al.* [52] in a Ni_2MnGa single crystal and he suggested the practicability of controlling the size of crystals by an external magnetic field. The demonstration of such a so-called FSMA was performed by Ullakko *et al.* [53]. This involves Ni_2MnGa, a Heusler-type alloy. Nowadays ferromagnetic shape memory alloys (FSMA) show clear changes with variation of an external magnetic field. Thereby changes in length of more than 10 % are possible. The Co-Ni-Al system attracts special attention as a potential candidate for the FSM effect due to certain features such as good oxidation resistance, low density and appreciable ductility at room temperature. The crystals were grown by the Bridgman method in [100] direction at different pulling rates [54, 55]. The present work studied austenitic [56] and martensitic [57] single crystals with nominal chemical composition $Co_{38}Ni_{33}Al_{29}$ by the X-ray Kossel diffraction and EBSD. Moreover, Kossel investigation on austenitic single- and polycrystalline FSMA Ni_2MnGa were started, see as example Fig. 2 on the right side.

4.2. Scanning electron microscopy and energy dispersive measurements

Figure 12 shows a typical backscattered electron micrograph of such a sample. In this investigated high-temperature austenitic state, we observe a two-phase structure of a matrix and second crystal phase of precipitates, which are marked with blue arrows. In order to investigate, whether the cause of the lower backscatter coefficient η at the grain boundaries in the matrix range can be explained with a change of the local chemical composition a lot of EDS mappings analysis of the element's Co-Kα, Ni-Kα and Al-Kα were carried out, for one example see Fig. 13. The EDS maps shows no clear change of the composition close to the phase boundary in the matrix. Initially, it only may be assumed, that the areas appear darker due to a better channelling effect on the basis of a higher crystal grade at the grain boundaries in the matrix range. This aspect could be clarified later by EBSD investigations and X-ray Kossel micro-diffraction.

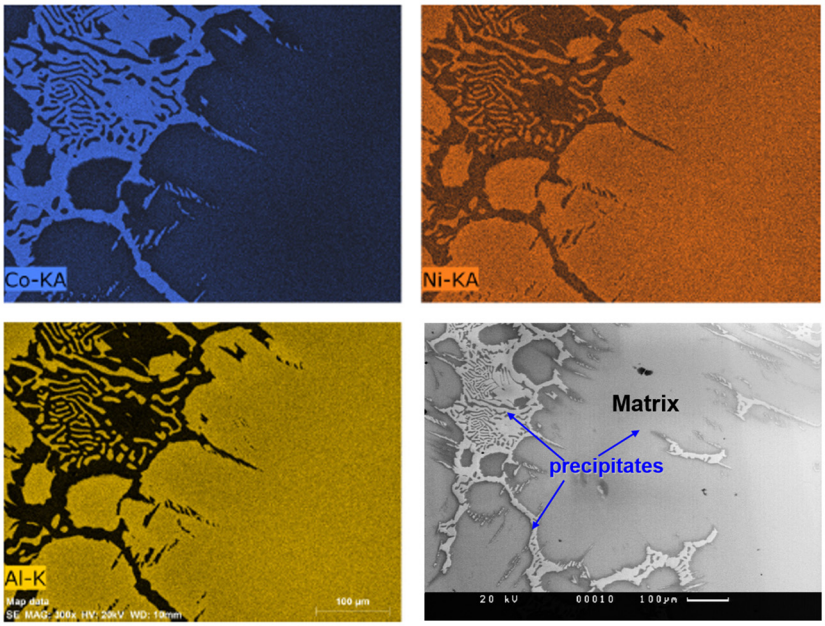

Figure 12. SEM micrograph of an austenitic $Co_{38}Ni_{33}Al_{29}$ alloy with matrix and some marked precipitates, a higher electron backscattering (lower backscatter coefficient η) was observed in the matrix range at the phase boundaries and EDS maps shows no composition change close to the phase boundary in the matrix.

4.3. Investigation of the crystal structure by means of Kossel X-ray diffraction

In such a ternary system Co-Ni-Al both the Co-$K\alpha_{1/2}$ and the Ni-$K\alpha_{1/2}$-radiation contributes to the Kossel diffraction, since the Al-$K\alpha_1$-radiation with a wavelength of $\lambda = 0.8339514$ nm is clearly to long wave in order to fulfil the Bragg equation. Therefore, all Kossel lines appears twice which means two identical reflection systems parallel to each other, please see Fig. 13, which shows a typical indexed Kossel pattern in the matrix range. Although the intensity is

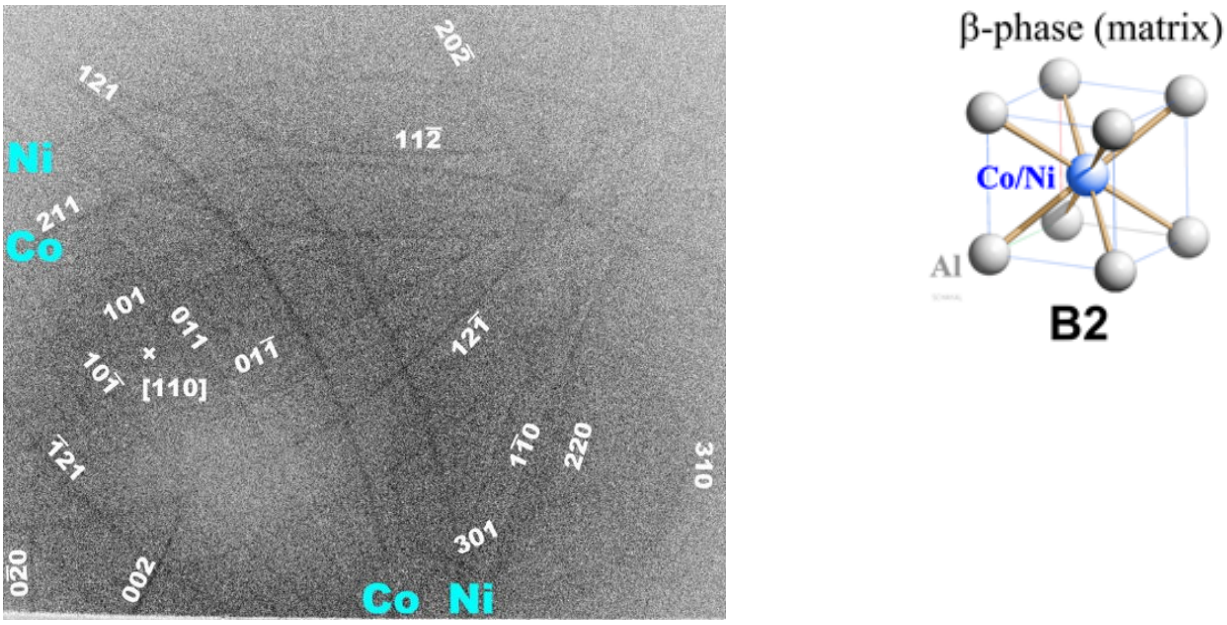

Figure 13. Left: Indexed Kossel pattern from the matrix, whereby the circular (310) Kossel reflection is remarkable, which is weak to see on the bottom right, and is due to the small opening angle very sensitive to lattice constant changes and could therefore be useful for precise local lattice constant determinations in the micro-range. Right: Sphere model of the matrix β-phase with B2 structure: only Co, Ni coloured in blue are statistically distributed.

separated for electron-excited Kossel X-ray interferences by 38 % for the Co-K$\alpha_{1/2}$-radiation as well as 33 % for the Ni-K$\alpha_{1/2}$-radiation, whereby the 29 at% Al atoms with the Al-K$\alpha_{1/2}$-radiation are not able to contribute, like discussed above, the Kossel pattern on the alloy Co-Ni-Al surprisingly have such an excellent quality. The both reflection systems are marked only for the 211 reflections with Co and Ni in light blue, whereby the Ni-radiation leads for each reflection to a larger Kossel cone opening angle than the Co-radiation. Only one of the both double reflections is indexed in each case. As a result of the evaluation of a variety of Kossel patterns the crystal structure in the matrix range could be determined independently to previous measurements with other methods, where an ordered matrix with the CsCl-structure type B2, space group Pm$\bar{3}$m (No. 221), was found [58], see Fig. 13 on the right side.

The following reflection types were observed in Kossel patterns of the matrix: 002, 011, 112, 022, and 103. Thereby, additional superstructure lines of the type 001, 111, 012 and 122 are necessary in order to prove the simple cubic structure. Not all superstructure lines could be clearly observed. Only the following lines could be unambiguous documented: type 001 and type 012, but the type 111 and 122 could not be detected. For one thing, the possible reason for this is that the ternary B2 phase $(A, C)_{1-x}B_x$ has with $(Co,Ni)_{71}Al_{29}$ not the ideally stoichiometric composition, then again the contrast ratios were relatively difficult in the corresponding Kossel patterns. The deviations of the ideal stoichiometric composition is with approximately 20 % very strong. The perpetuation of the B2 structure is only possible by the formation of

an enormous number of so-called constitutional crystal defects, whereby two kinds of point defects are important for ordered alloys: antistructure atoms and vacancies [59, 60], which can possibly explain the missing reflections.

4.4. First explanation of observed unusual X-ray Kossel reflection doubling

In earlier Kossel measurements of other materials a doubling of Kossel reflections where already observed by other authors, but also from our group both at tensile deformed fcc Ni crystals and at fcc Cu bicrystals, but the cause could not yet be elucidated in the past. Figure 14 shows two typical observed X-ray Kossel patterns at different positions in the γ-phase in austenitic $Co_{38}Ni_{33}Al_{29}$ single crystals. Initially, in both patterns the doubling of each line with a large distance can be seen, which means a relatively big difference in the opening angles (90° - ϑ_B) of the cones, only this can be easily explained by the excited two different radiations Co- and Ni-$K\alpha_{1/2}$, which leads to two parallel reflection systems, whereby the $K\alpha_{1/2}$-doublet could not be resolved. In the left pattern of Fig. 14 it can be seen, that the reflections are more directly overlapped and the distances between doubled lines are very small (marked with yellow arrows), especially more on the left side of the reflection from the lower left to the top right, which leads here also to a higher intensity and a kind of broadening of these reflections more on the right side. On the other right side of Fig. 14, one can see larger distances between the Kossel line, which lead to a very clear and precise splitting in two reflections (also marked with yellow arrows). Additionally, a remarkable circular Kossel reflection appears in both Kossel patterns, but more clearly on the right side of Fig. 14. The observed Kossel reflection doubling could be explained by an abnormal overlapping of Kossel reflections of two different crystal phases, for the first time. Whereby several other reasons could be excluded. Initially, especially it was very difficult to index the above-mentioned circular Kossel reflection, which lies asymmetric to the γ-crystal phase and, therefore, seems not to come from the same crystal lattice. In detail almost all reflection in the patterns can be assigned to the A1 γ-phase and additionally the strongest reflections mainly of the {0 1 1} type can be observed from the second crystal β-phase B2 of the matrix, which can explain the reflection doubling, first. Moreover, it was found that the circular Kossel reflection belongs also to the β-phase, more details in the next section.

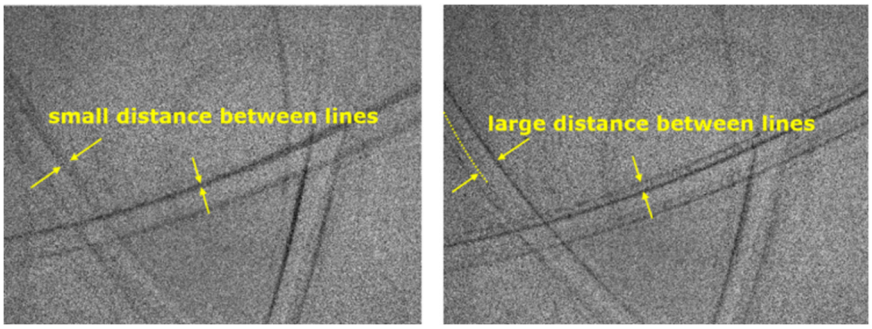

Figure 14. X-ray Kossel micro diffraction patterns in the γ-phase with different unusual measured doubling of reflections in this case in austenitic $Co_{38}Ni_{33}Al_{29}$, which could be explained here for the first time and with high probability similar reflections doubling, which were observed of other groups in the past; with 013 circle reflection of the matrix.

4.5. Development of a novel method for the determination of the orientation relationships using the reflection doubling of just one Kossel pattern and its application for Co-Ni-Al

Figure 15 shows a manifold superposition of Kossel reflections, which means also a second doubling of only the Kossel lines of the 110_{B2}-reflection with a very small difference in the opening angles of the cones, which has been observed for the first time in Kossel patterns of this Co-Ni-Al alloy [56]. As a result, it has been experimental succeeded to find a pattern geometry, where instead of just the pure reflection doubling a second complete reflections system was observable, see Fig. 15. This second reflection system could be assigned to the matrix B2-phase. Thus, the reflections $0\ 1\ 1_{B2}$, $1\ 0\ \bar{1}_{B2}$, $\bar{1}\ 0\ \bar{1}_{B2}$, $0\ 0\ \bar{2}_{B2}$ could be indexed in Fig. 15, whereby clearly the double reflection to the reflection $1\ 1\ 1_{A1}$ of the precipitates phase could be identified as reflection $1\ 1\ 0_{B2}$ [56]. This one exists exactly like the $1\ 1\ 1_{A1}$ and the $0\ 0\ 2_{A1}$ twice both for Co- and for Ni-Kα.

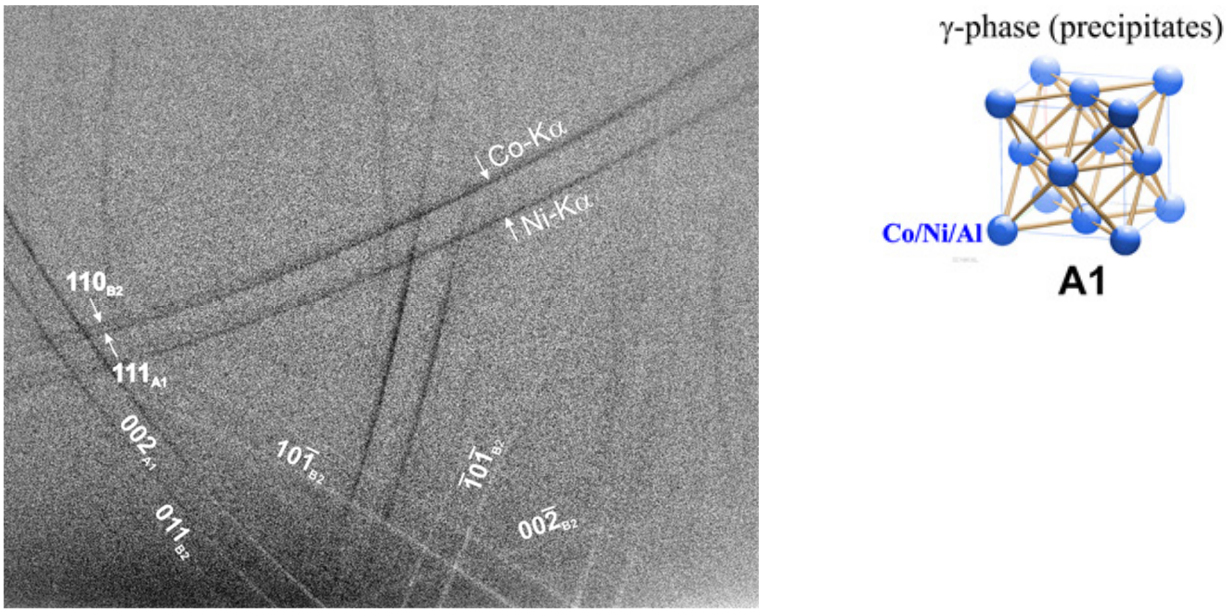

Figure 15. Left: X-ray Kossel Diffraction pattern of the shape memory alloy Co-Ni-Al at the matrix close to the phase boundary. Overlaps of two reflection systems between the B2 and A1 crystal phases can be seen, which were used to develop a novel fast method for the determination of orientation relationships using just one Kossel pattern [56]. Right: Sphere model of the A1 (fcc) structure of the measured γ-phase of the precipitates.

Overlaps of Kossel reflections of two different crystal phases were observed. In the cubic case principally all Kossel cones lies vertical to the corresponding lattice planes. This fact and the directions of the Kossel cones are illustrated in the schematic sketch of Fig. 16. The $(111)_{A1}$ lattice planes belongs to the $(111)_{A1}$ Kossel cone (both marked in blue). Thus we can easily imagine, that if the both overlapped indexed Kossel cones $(111)_{A1}$ of the fcc phase of the

precipitates (A1) and the $(110)_{B2}$ Kossel cone of the matrix (B2) lies in the same cone axis direction, which is the case if the reflections are exactly parallel to each other (see Fig. 16) that automatically the lattice planes belonging to it have to be precisely parallel.

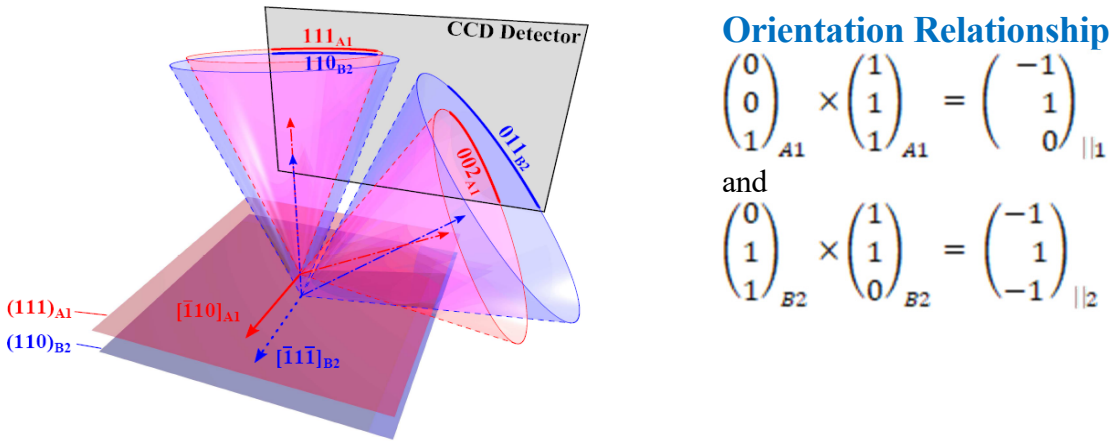

Figure 16. Simplified representation of the geometric arrangement of Kossel cones [56].

With this a fast and easy new method could be found to directly determine that the two planes lie parallel to each other and thereby their plane orientation relationship using just one Kossel pattern. The result is the following relationship between the planes, see Fig. 16: $\mathbf{(111)}_{A1} \parallel \mathbf{(110)}_{B2}$ [56]. Hereby, the determined misorientation lies within a few 0.1° and Kossel measurements reveals areas of excellent crystal quality with a very low dislocation density < 10^{-7} cm^{-2} along the phase boundary. The next point would be to determine the rotation of both planes to each other. For this one needs to determine two crystal orientations pointing in the same direction. If one realises in the reciprocal space that the cone axis of the $(111)_{A1}$ Kossel cone and the $(001)_{A1}$ cones axis of the $(002)_{A1}$ Kossel cone lies in one plane which is perpendicular to the searched directions, than one can found an easy way in order to determine the orientation direction just by evaluation of two simple cross products of the Kossel cone axis in the correct order in Fig. 16. With the two vector products of the cone normals the crystal orientation was calculated in each case, which points in the same direction. The total result allowed to determine precisely the Kurkjumov-Sachs [61] orientation relationship:

$$\mathbf{(1\,1\,1)_{A1} \parallel (1\,1\,0)_{B2}} \quad \text{and} \quad \mathbf{[\bar{1}\,1\,0]_{A1} \parallel [\bar{1}\,1\,\bar{1}]_{B2}} \text{ [56]},$$

which is in agreement with other more extensive electron diffraction measurements by transmission electron microscopy, in the literature for this special material [62].

6. CONCLUSIONS AND OUTLOOK

First Kossel measurements on a potential candidate for the ferromagnetic shape memory effect and a second FSMA Ni_2MnGa were presented. With the applications shown and the results, which were discussed, the great performance of the Kossel method turned out. Moreover, in the last 20 years considerable progress was achieved to overcome the following major disadvantages: Not only the CCD area detector replaced the X-ray film, but also the first successful steps have been taken in direction of the automated indexing of X-ray Kossel patterns by Maurice and Fortunier (2008) in Saint-Étienne, France [63]. Beside, these, a further new approach lies in the application of focal curves by Henschel and Bauch (2013) in Dresden [64]. Moreover, new Kossel simulation programmes were developed from different groups especially KSLSTRAIN by Morawiec [65], by Bortel *et al.* [66], which notably simplified and extended the evaluation.

7. ACKNOWLEDGEMENTS

I would like to thank the colleagues Carsten Schurig, Leonid P. Potapov, Katerina Krátká, M.N. Melo and Jaromír Kopeček for their contributions to the results presented here. We are grateful to Robert Chulist for providing the Ni_2MnGa samples.

8. REFERENCES

[1] Kossel W 1924 *Z. Physik* **23** 278
[2] Kossel W, Loeck V and Voges H 1935 *Z. Physik* **94** 139
[3] Kossel W 1937 *Erg. exakt. Naturwiss.* **16** 295-352
[4] Borrmann G 1935 *Naturwiss.* **23** 591; 1936 *Ann. Phys. (Leipzig)* **27** 669
[5] Geist V and Flagmeyer R 1974 *phys. stat. sol. (a)* **26** K1
[6] Roberto J B, *et al.* 1975 *J. Appl. Phys.* **46** 936
[7] Ullrich H-J, *et al.* 1994 *Nucl. Instrum. Methods Phys. Res. A* **349** 269
[8] Schetelich C, *et al.* 1995 *Nucl. Instrum. Methods. Phys. Res. B* **103** 236
[9] Langer E, Däbritz S, Hauffe W and Haschke M 2005 *Appl. Surf. Sci.* **252** 240
[10] Langer E, Haschke M and Däbritz S 2008 *Mikrochimica Acta* **161** 455
[11] Peyrusse O, Jonnard P, Le Guen K and André J-M 2020 *Phys. Rev. A* **101** 013818
[12] von Laue M 1960 *Röntgenstrahl-Interferenzen*. [Frankfurt am Main, Germany: Akademische Verlagsgesellschaft]
[13] Goehner M and Michael J R 1995 *Adv. X-ray Anal.* **38** 539
[14] Ullrich H-J, *et al.* 1998 *HASYLAB annual report*. [Hamburg, Germany: HASYLAB] 887-888
[15] Däbritz S, Langer E and Hauffe W 1999 *J. Anal. Atom. Spectrom.* **14** 409
[16] Däbritz S, Langer E and Hauffe W 2001 *Appl. Surf. Sci.* **179** 38

[17] Langer E, Däbritz S, Schurig C and Hauffe W 2001 *Appl. Surf. Sci.* **179** 45
[18] Wilkinson A J, Meaden G and Dingley D J 2006 *Ultramicroscopy* **106** 307
[19] Wilkinson A J, Meaden G and Dingley D J 2006 *Mater. Sci. Technol.* **22** 1271
[20] Winkelmann A, Schröter B and Richter W 2004 *Phys. Rev. B* **69** 245417
[21] Winkelmann A, *et al.* 2007 *Ultramicroscopy* **107** 414
[22] Nolze G, Grosse C and Winkelmann A 2015 *J. Appl. Crystallogr.* **48** 1405
[23] Ullrich H-J, Thiele K, Däbritz S, Schreiber H and Götze K 1972 *Krist. Techn.* **7** 1153
[24] Bauch J, *et al.* 1999 *Cryst. Res. Technol.* **34** 71
[25] Brechbühl J, Bauch J and Ullrich H-J 1999 *Cryst. Res. Technol.* **34** 59
[26] Böhling M, Bauch J and Ullrich H-J 2009 *Cryst. Res. Technol.* **44** 1185
[27] Nolze G, Winkelmann A, Cios G and Tokarski T 2021 *Mater. Charact.* **175** 111040
[28] von Laue M 1935 *Naturwiss.* **23** 373
[29] von Laue M 1935 *Ann. Phys.* **23** 705
[30] Ott H 1938 *Ann. Phys.* **31** 264
[31] Blau W, Schreiber H, Schulze G E R and Ullrich H-J 1967 *Naturwiss.* **54** 535
[32] Stephan D, Blau W, Ullrich H-J and Schulze G E R 1974 *Krist. Techn.* **9** 707
[33] Stephan D, Ullrich H-J and Schulze G E R 1976 *Krist. Techn.* **11** 475
[34] Brümmer O and Nieber J 1975 *Mikrochimica Acta* **Suppl. 6** 345
[35] Hutton J T, *et al.* 1985 *Phys. Rev. B* **31** 743
[36] Faigel G, Bortel B and Tegze M 2016 *Sci. Rep.* **6** 22904
[37] Brümmer O, Beier W and Nieber J 1973 *phys. stat. sol. (a)* **20** K119
[38] Geist V and Flagmeyer R 1974 *phys. stat. sol. (a)* **26** K1
[39] Ullrich H-J, Schatt W, Däbritz S and Geist V 1977 *Microchimica Acta* **Suppl. II** 167
[40] Nolze G, Geis V, Wagner G, Paufler P and Jurkschat K 1990 *Z. Kristallogr.* **193** 111
[41] Ullrich H-J, *et al.* 1983 *Mikrochimica Acta* **Suppl. I** 175
[42] Herenz A, *et al.* 1984 in: *Proc. 6th Microprobe Conf. (Dresden)*. [Phys. Soc. of GDR] 203
[43] Däbritz S 1974 *PhD Thesis*. [Dresden, Germany: Dresden University of Technology]
[44] Ullrich H-J, Däbritz S and Schreiber H 1968 in: *Proc. 5th International Congr. on X-Ray Optics and Microanalysis (Tübingen)* (Möllenstedt G and Gaukler K H; Eds.) 406-411
[45] Ullrich H-J 1967 *PhD Thesis*. [Dresden, Germany: Dresden University of Technology]
[46] Richter K, *et al.* 1997 *Mikrochimica Acta* **125** 115
[47] Kurt R, Däbritz S, *et al.* 1997 *Defect and Diffusion Forum* **143-147** 609
[48] Langer E, Kurt R and Däbritz S 1999 *Cryst. Res. Technol.* **34** 801
[49] Däbritz S, Hauffe W and Kurt R 1997 *Mikrochimica Acta* **125** 3-12
[50] Bouscaud D, *et al.* 2014 *Adv. Mater. Res.* **996** 45
[51] Pesci P, *et al.* 2006 *Mater. Sci. Forum* **524-525** 109-114
[52] Vasil'ev A N, Klestov S A, Levitin R Z and Snegirev V V 1996 *J. Exp. Theor. Phys.* **82** 524
[53] Ullakko K, *et al.* 1996 *Appl. Phys. Lett.* **69** 1966
[54] Kopeček J, *et al.* 2009 in: *ESOMAT 2009 - 8th Eur. Symp. Martensitic Transformations.* (Šittner P, Paidar V, Heller L and Seiner H; Eds.) [Les Ulis, France: EDP Sciences] 02013

[55] Kopeček J, *et al.* 2010 *IOP Conf. Series: Mat. Sci. Eng.* **7** 012013
[56] Langer E, Potapov L, Melo M N and Kopeček J 2023 in preparation
[57] Langer E, Krátká K, Kopeček J and Richter A 2023 in preparation
[58] Hubert-Protopescu M and Hubert H 1991 *Aluminium-cobalt-nickel ternary alloys: a comprehensive compendium of evaluated constitutional data and phase diagram. Vol. 4: Al-Cd-Ce to Al-Cu-Ru*. (Petzow G and Effenberg G; Eds.) [Weinheim, Germany: VCH] 234
[59] Grün A, Henig E-T and Sommer F 1998 *Z. Metallkd.* **89** 591
[60] Breuer J, *et al.* 2001 *Metall. Mater. Trans. A* **32** 2157
[61] Kurdjumow G and Sachs G 1930 *Z. Phys.* **64** 325
[62] Bartova B, *et al.* 2007 *Scripta Materialia* **57** 37
[63] Maurice C and Fortunier R 2008 *J. Microscopy* **230** 520
[64] Henschel F and Bauch J 2013 *J. Geom. Graphics* **17** 205
[65] Morawiec A 2016 *J. Appl. Cryst.* **49** 322
[66] Bortel G, Tegze M and Faigel G 2021 *J. Appl Cryst.* **54** 123-131